Using Machine Learning Techniques for Data Quality Monitoring at CMS Experiment

by

Guillermo A. Fidalgo Rodríguez

A thesis presented for the degree of

BACHELLOR'S OF SCIENCE??

in

Physics

UNIVERSITY OF PUERTO RICO
MAYAGÜEZ CAMPUS
2018

Approved by:

Sudhir Malik, Ph.D. President, Graduate Committee	Date
Héctor Méndez, Ph.D. Member, Graduate Committee	Date
Samuel Santana Colón, Ph.D. Member, Graduate Committee	Date
Rafael A. Rámos, Ph.D. Chairperson of the Department	Date

Abstract

The Data Quality Monitoring (DQM) of CMS is a key asset to deliver high-quality data for physics analysis and it is used both in the online and offline environment. The current paradigm of the quality assessment is labor intensive and it is based on the scrutiny of a large number of histograms by detector experts comparing them with a reference. This project aims at applying recent progress in Machine Learning techniques to the automation of the DQM scrutiny. In particular the use of convolutional neural networks to spot problems in the acquired data is presented with particular attention to semi-supervised models (e.g. autoencoders) to define a classification strategy that doesn't assume previous knowledge of failure modes. Real data from the hadron calorimeter of CMS are used to demonstrate the effectiveness of the proposed approach.

Keywords: [DQM, online, offline, Machine Learning]

Acknowledgments

I wish to thank United States State Department and University of Michigan for providing the opportunity to work abroad at CERN during the 2018 Winter Semester. I also wish to thank CERN staff, CMS Experiment , Texas Tech University, and the University of Puerto Rico at Mayagüez, with special thanks to Dr. Federico de Guio for his local mentorship and Dr. Nural Akchurin, and Dr. Sudhir Malik for their guidance. A very special thanks to Dr. Jean Krisch for accepting me for this great research opportunity and Dr. Steven Goldfarb for being a wonderful host and overall local guidance at CERN.

List of Figures

Contents

Chapter 1

Introduction

The work for this thesis was performed at CERN on CMS Experiment. CERN stands for European Organization for Nuclear Research. It was founded in 1954 and is located at the Franco-Swiss border near Geneva. At CERN, physicists and engineers are probing the fundamental structure of the universe. They use the world's largest and most complex scientific instruments to study the basic constituents of matter – the fundamental particles. The instruments used at CERN are purpose-built particle accelerators and detectors. Accelerators boost beams of particles to high energies before the beams are made to collide with each other or with stationary targets. Detectors observe and record the results of these collisions. The accelerator at CERN is called the Large Hadron Collider (LHC), the largest machine ever built by humans and it collides particles (protons) at close to the speed of light. The process gives the physicists clues about how the particles interact, and provides insights into the fundamental laws of nature. Seven experiments at the LHC use detectors to analyze particles produced by proton-proton collisions. The biggest of these experiments, ATLAS and CMS, use general-purpose detectors designed to study the fundamental nature of matter and fundamental forces and to look for new physics or evidence of particles that are beyond the Standard Model. Having two independently designed detectors is vital for cross-confirmation of any new discoveries made. The other two major detectors ALICE and LHCb, respectively, study a state of matter that was present just moments after the Big Bang and preponderance of matter than antimatter. Each experi-

ment does important research that is key to understanding the universe that surrounds and makes us.

Chapter 2 presents a basic description of the Large Hadron Collider and CMS Detector

?? gives a brief motivation

?? is dedicated to a study optimizing

?? ptimated.

?? details an improvarger production cross-section than Z+jets process used before.

The conclusions and results of each chapter are presented in the corresponding chapter.

This thesis work has been presented at several internal meetings of the CMS Experiment and at the following international meetings and conferences:

1. **Andrés Abreu** gave a talk "***Estimation of the Z Invisible Background for Searches for Supersymmetry in the All-Hadronic Channel***" at "APS April 2018: American Physical Society April Meeting 2018, 14-17 Apr 2018", Columbus, OH

2. **Andrés Abreu** gave a talk "***Phase-2 Pixel upgrade simulations***" at the "USLUA Annual meeting: 2017 US LHC Users Association Meeting, 1-3 Nov 2017", Fermilab, Batavia, IL

Chapter 2

The CMS Experiment

The Compact Muon Solenoid (CMS) detector is a general purpose particle detector designed to investigate various physical phenomena concerning the SM and beyond it, such as Supersymmetry, Extra Dimensions and Dark Matter. As its name implies, the detector is a solenoid which is constructed around a superconducting magnet capable of producing a magnetic field of 3.8 T. The magnetic coil is 13m long with an inner diameter of 6m, making it the largest superconducting magnet ever constructed. The CMS detector itself is 21m long with a diameter of 15m and it has a weight of approximately 14,000 tons. The CMS experiment is one of the largest scientific collaborations in the history of mankind with over 4,000 participants from 42 countries and 182 institutions. CMS is located at one of these points and it essentially acts as a giant super highspeed camera that makes 3D images of the collisions that are produced at a rate of 40 MHz (40 million times per second). The detector has an onion-like structure to capture all the particles that are produced in these high energy collisions most of them being unstable and decaying further to stable particles that are detected. CMS detector was designed with the following features (as shown in Figure 2.1) :

1. A **magnet** with large bending power and high performance muon detector for good muon identification and momentum resolution over a wide range of momenta and angles.

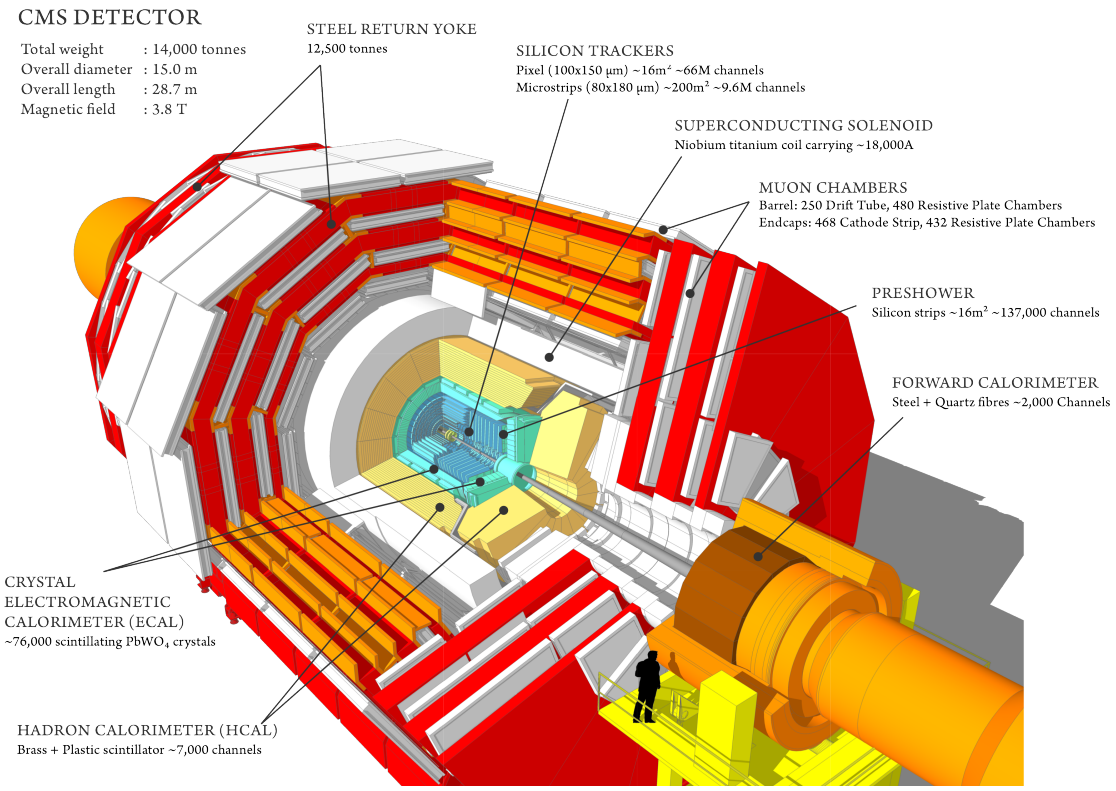

Figure 2.1: CMS Detector

2. An **inner tracking system** capable of high reconstruction efficiency and momentum resolution requiring **pixel detectors** close to the interaction region.

3. An **electromagnetic calorimeter** able to provide good electromagnetic energy resolution and a high isolation efficiency for photons and leptons.

4. A **hadron calorimeter** capable of providing precise missing-transverse-energy and dijet-mass resolution.

A property from these particles that is exploited is their charge. Normally, particles produced in collisions travel in a straight line, but in the presence of a magnetic field, their paths are skewed and curved. Except the muon system, the rest of the subdetectors lie inside a 3.8 Tesla magnetic field . Due to the magnetic field the trajectory of charged particle produced in the collisions gets curved (as shown in Figure 2.2) and one can calculate the particle's momentum and know the type of charge on the particle. The Tracking devices are responsible for drawing the trajectory of the particles by using a computer program that reconstructs the path by using electrical signals that are left by

the particle as they move. The Calorimeters measure the energy of particles that pass through them by absorbing their energy with the intent of stopping them. The particle identification detectors work by detecting radiation emitted by charged particles and using this information they can measure the speed, momentum, and mass of a particle. After the information is put together to make the "snapshot" of the collision one looks for results that do not fit the current theories or models in order to look for new physics.

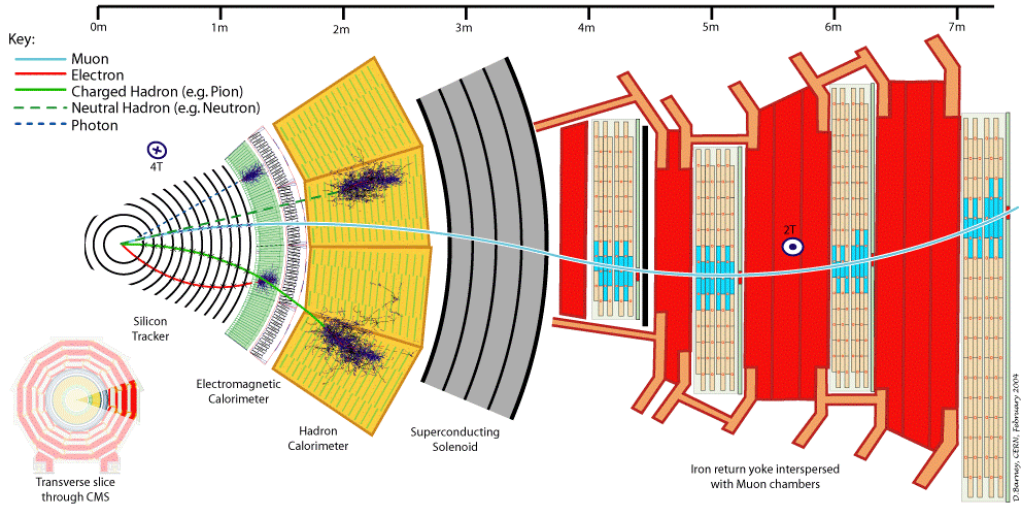

Figure 2.2: The trajectory of a particle traveling through the layers of the detector leaving behind it's signature footprint

The project focusses specifically on data collected from one of the Calorimeters, - the Hadron Calorimeter (HCAL). The HCAL, as its name indicates, is designed to detect and measure the energy of hadrons or, particles that are composed of quarks and gluons, like protons and neutrons. Additionally, it provides an indirect measurement of the presence of non-interacting, uncharged particles such as neutrinos (missing energy) . Measuring these particles is important as they can tell us if new particles such as the Higgs boson or supersymmetric particles (much heavier versions of the standard particles we know) have been formed. The layers of the HCAL are structured in a staggered fashion to prevent any gaps that a particle might pass through undetected. There are two main parts: the barrel and the end caps. There are 36 barrel wedges that form the last layer of the detector inside the magnet coil, there is another layer outside this, and on the endcaps, there are another 36 wedges to detect particles that come out at shallow angles with respect to the beam line.

Chapter 3

Data Collection and Data Quality Monitoring

3.1 What is Data Collection for CMS?

During data taking there are millions of collisions occurring in the center of the detector every second. The data per event is around one million bytes (1 MB), that is produced at a rate of about 600 million events per second [1], that's about 600 MB/s. Keeping in mind that only certain events are considered "interesting" for analysis, the task of deciding what events to consider out of all the data collected is a two-stage process. First, the events are filtered down to 100 thousand events per second for digital reconstruction and then more specialized algorithms filter the data even more to around 100 200 events per second that are found interesting. For CMS there is a Data Acquisition System that records the raw data to what's called a High-Level Trigger farm which is a room full of servers that are dedicated to processing and classify this raw data quickly. The data then gets sent to what's known as the Tier-0 farm where the full processing and the first reconstruction of the data are done. [2]

3.2 What is Data Quality Monitoring?

To operate a sophisticated and complex apparatus as CMS, a quick online feedback on the quality of the data recorded is needed to avoid taking low quality data and to guarantee a good baseline for the offline analysis. Collecting a good data sets from the collisions is an important step towards search for new physics as deluge of new data poses an extra challenge of processing and storage. This all makes it all the more important to design algorithms and special software to control the quality of the data. This is where the Data Quality Monitoring (DQM) plays a critical in the maintainability of the experiment, the operation efficiency and performs a reliable data certification. The high-level goal of the system is to discover and pinpoint errors, problems occurring in detector hardware or reconstruction software, early, with sufficient accuracy and clarity to maintain good detector and operation efficiency. The DQM workflow consists of 2 types: **Online** and **Offline**.

The **Online** DQM consists of receiving data taken from the event and trigger histograms to produce results in the form of monitoring elements like histogram references and quality reports. This live monitoring of each detector's status during data taking gives the online crew the possibility to identify problems with extremely low latency, minimizing the amount of data that would otherwise be unsuitable for physics analysis. The scrutiny of the Online DQM is a 24/7 job that consists of people or shifters that work at the CMS control center constantly monitoring the hundreds of different plots and histograms produced by the DQM software. This consumes a lot of manpower and is strenuous work.

The **Offline** DQM is more focused on the full statistics over the entire run of the experiment and works more on the data certification. In the offline environment, the system is used to review the results of the final data reconstruction on a run-by-run basis, serving as the basis for certified data used across the CMS collaboration in all physics analyses. In addition, the DQM framework is an integral part of the prompt calibration loop. This is a specialized workflow run before the data are reconstructed to compute and validate the most up-to-date set of conditions and calibrations subsequently used during

the prompt reconstruction.

This project aims to minimize the DQM scrutiny by eye and automate the process so that there is a more efficient process to monitor the detector and the quality of the data by implementing Machine Learning techniques.

Chapter 4

What is Machine Learning?

Machine Learning (ML) can be defined as an application of Artificial Intelligence that permits the computer system to learn without being told explicitly. In ML a computer program is said to learn from experience E with respect to some class of tasks T and performance measure P, if its performance at tasks in T, as measured by P, improves with experience E [3]. ML has made tremendous strides in the past decades and has become very popular recently due to its multifaceted applications. It is being used on social media, marketing, and in the scientific community as well. Some examples of ML applications are: the algorithms used on application in smartphones to detect human faces, self-driving cars, computer games, stock prediction, and voice recognition. An interesting characteristic of ML algorithms is that the more data one inputs the better is the performance. The ML application has a very wide spectrum covering almost every aspect of human endeavor that involves a lot of data. Scientific analysis today generates enormous data and is a hence is a perfect used case to apply ML techniques. In this work we use enhanced ML techniques based on progress in the recent past.

In general, there are two main categories to classify machine learning problems: **Supervised Learning** (SL) and **Unsupervised Learning** (UL). SL is the most used ML approach and has proven to be very effective for a wide variety of problems. Examples of common SL problems are: spam filters, predicting housing prices, identifying a malignant or benign tumor, etc. These types of problems are characterized by providing a

"right answer" as a reference. For example, spam filter algorithms identify emails that are spams by training on a dataset that has examples of such emails. In case of predicting house prices, the algorithm is trained on a dataset of houses involving features like the area of the house, number of rooms, and the selling price of the house.

UL algorithms are different in the sense that they do not have the "right answers" given to the machine. Instead, UL algorithms are used for finding patterns and make clusters from the given data. That is what also forms the basis of a search engine (e.g. Google news). Clicking on a link to a news article, one gets many different stories of different journals that have some correlation with the article searched. This happens because the ML algorithm is capable of learning features and shared patterns from a bunch of data without being given any specifics. Another interesting UL problem is the so-called "cocktail party" that involves distinguishing the voice of two people recording on two microphones located at different places. The ML algorithm is able to separate the sources of the voices in the recordings by learning the voice features that correspond to each person, showing the power of the UL algorithm.

In this study, I have focused on an SL approach and a variant of the UL approach, called the **Semi-Supervised Learning** approach (SSL). The SSL is named so because the data involves looking at images that are already known to be "Good" but one doesn't necessarily know every possible situation that produces a "Bad" image. The purpose is to define a metric for a "good" image and subsequently decide if an image is "bad" in case it deviates too much from an acceptable value.

4.1 Developing the Algorithm

To develop an ML algorithm the following are taken into consideration, what is the task? and what is the method to approach the task? In our case, we are looking into images that have information about the activity that the channels in the HCAL are detecting. These images are called "occupancy maps" and they are a visual way of monitoring the health of the detector itself (see Figure 4.1). There are two common problems that can be

identified by viewing occupancy maps which are called ”dead channels” and ”hot towers”. They are referred to as “**dead**” and “**hot**” respectively in the rest of this document. Dead channels mean that on a certain place in the occupancy map there is not any readout from the channels on the HCAL and hot channels mean that there are channels that are being triggered by noise or are damaged in a way that makes them readout too much activity.

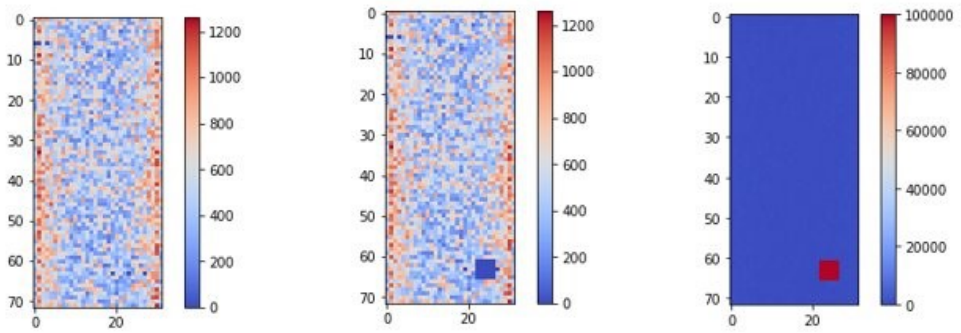

(a) Good Image **(b)** Dead Image **(c)** Hot Image

Figure 4.1: Occupancy maps with 5x5 affected regions

The problem is the following, to create a model that can detect and classify what type of scenario is occurring on each occupancy map. For this, we want to go with a SL approach which means that we will give the model the images as the input and it will train on these images by learning to identify patterns or features in the image and try to do a “fit” from the images to their corresponding labels. After the training, the algorithm will be given a testing set for us to evaluate the model’s ability to correctly detect if there is a problem with the image and what type of problem is being detected. The output of the model will be the predicted class of the test image. The predictions are based on the labels and their corresponding images that were given to the model during training. This means that if the model was trained with 3 different types of images with their corresponding label the model will only work well for images that present similar patterns or characteristics to those presented in the training. For example, if we only train the model to distinguish between “good” and “hot” then when the model encounters images that aren’t either of these two, like an image labeled “dead”, then the model will not know what to do with this image and will give it an incorrect label. After the SL model has been tested the next step is trying an SSL model. The term semi-supervised

simply means that there isn't a ground truth label that is being given to the model during training because either there isn't necessarily a ground truth, or we don't know what the ground truth is. What we do know, is what is considered as a "good" image and what this approach hopes to accomplish is to use the error in the reconstruction of the input image and use that information to discriminate between the "good" vs the "bad" images.

4.2 Teaching the Algorithm

The way an ML algorithm learns is by an iterative process called an optimization algorithm in which the predicted output value of the model is compared to the desired output (See Figure 4.2) and the weights and biases of the model are adjusted such that the predicted output is closer to the desired output.

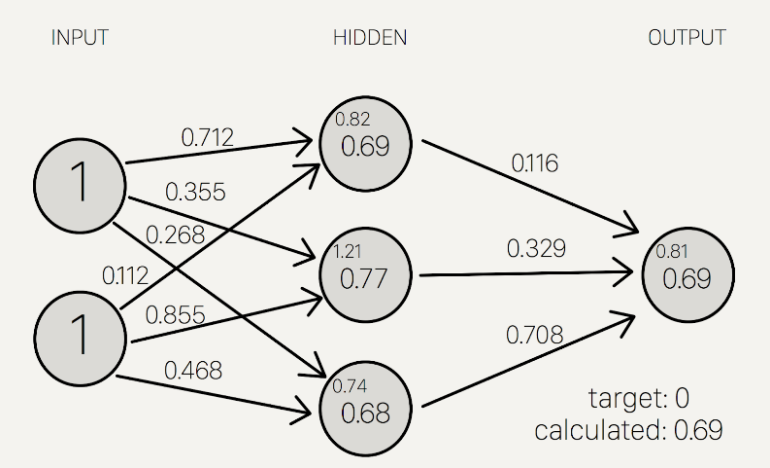

Figure 4.2: Weights and Biases

"Optimization algorithms helps us to **minimize** (or **maximize**) an **Objective** function *(another name for **Error** function)* **E(x)** which is simply a mathematical function dependent on the Model's internal **learnable parameters** which are used in computing the target values(**Y**) from the set of *predictors*(**X**) used in the model. For example - we call the **Weights(W)** and the **Bias(b)** values of the neural network as its internal learnable *parameters* which are used in computing the output values and are learned and updated in the direction of optimal solution i.e. minimizing the **Loss** by the network's training process and also play a major role in the ***training*** process of the Neural Network Model." [4].

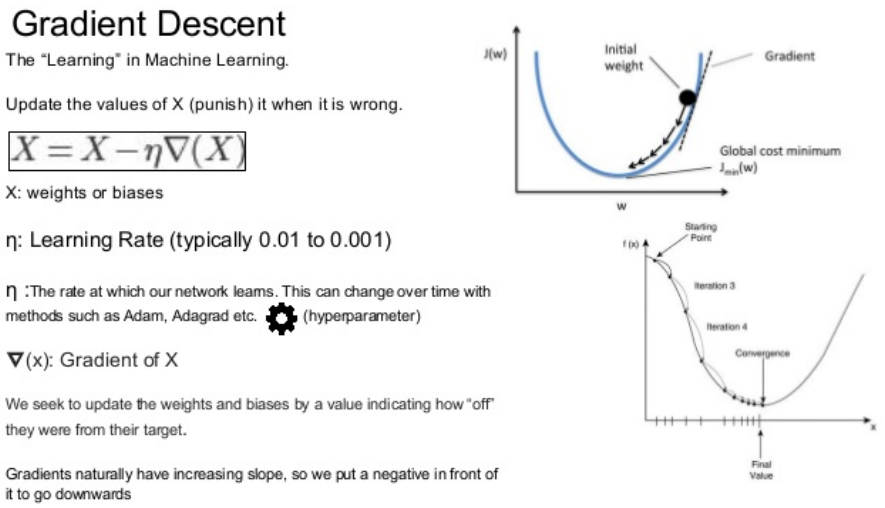

Figure 4.3: Gradient Descent algorithm

The most basic and probably the most used optimizer is called Gradient Descent (GD). GD is based on the concept of using the gradient of a loss or cost function and moving the weights and biases of the ML model so that the predicted value is taking a step in the decreasing direction of this error function (See Figure 4.3). In general, the "terrain" of the loss function is not a smooth bowl-shaped surface like the one present in the image. The most general form of the surface is more similar to a rocky mountain (See Figure 4.4), which presents a problem when using simple optimizers like GD.

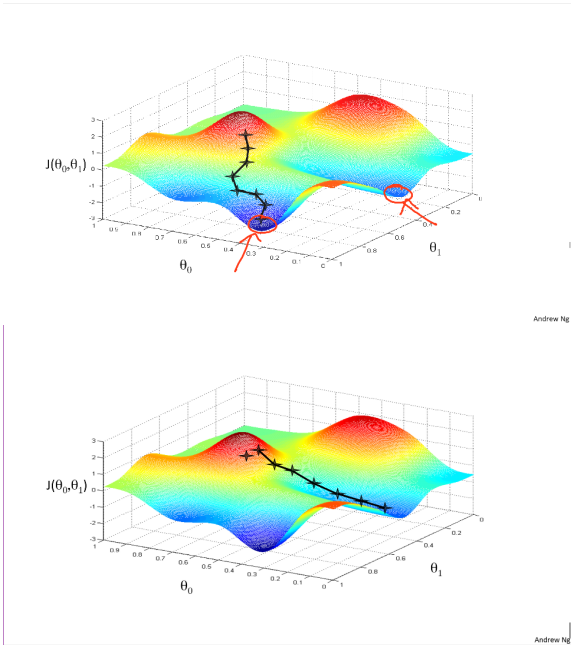

Figure 4.4: Loss Function surface

Chapter 5

Results

5.1 Introduction

A detailed explanation for the estimation of the Z$\rightarrow \nu\bar{\nu}$+jets background is presented in this chapter. The following estimation procedure builds upon the 2016 SUSY analysis summarized in **??** and aims to refine the overall background calculation as well as reduce the uncertainties associated with the previous method. To accomplish this, an additional γ+jets CS is used in conjunction with the tight Z$\rightarrow \mu^+\mu^-$ control region used in the 2016 analysis estimation. The new γ+jets CS provides a more data-driven estimation procedure with the added benefit of a substantially larger production cross-section than Z+jets processes [**?**].

5.2 The Irreducible Z$\rightarrow \nu\bar{\nu}$ Background

An important source of background in searches for SUSY in the 0-lepton final state comes from events in which a Z boson, accompanied by jets, decays into a pair of neutrinos (Z$\rightarrow \nu\bar{\nu}$+jets). The resulting final state is comprised of a large p_{T}^{miss} (from the neutrino pair) and multiple hadron jets, closely mimicking the SUSY signal. For similar searches, the Z$\rightarrow \nu\bar{\nu}$ contribution can make up a large portion of the background in many of the search bin regions (higher than 50% in some regions) [**?**, **?**], and can compose up

to about a third of the total SM background. For this particular analysis, the Z$\rightarrow \nu\bar{\nu}$ accounts for about 17% of the total SM background and owes its low value to the dedicated top-tagging algorithm outlined in **??**.

There are several different methods that have been developed to estimate the Z$\rightarrow \nu\bar{\nu}$+jets background [**?**]. Two of the commonly used methods involve the use of a control region dominated by Z$\rightarrow ll$+jets, where the l stands for lepton (either a muon or an electron, in this case) or γ+jets events. The Z$\rightarrow ll$ channel has the advantage of having very similar kinematics to the Z$\rightarrow \nu\bar{\nu}$ region but suffers from low statistics (due in part to its small branching ratio), specially in the tight search regions used in typical SUSY searches. On the other hand, the γ+jets region has a much higher production cross-section but involves a completely different process. The hybrid method described in this chapter makes use of both control regions in order to estimate the Z$\rightarrow \nu\bar{\nu}$ background corrections, and aims to improve on the results of the 2016 method described in **??**.

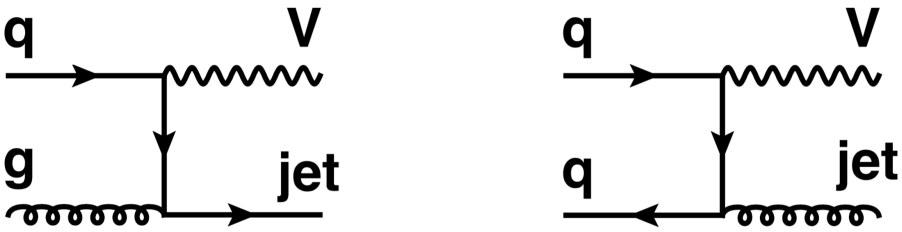

Figure 5.1: Leading-order Feynman diagrams for Z+ jets and γ+ jets processes. The 'V' in the figure can represent either Z or γ.

5.3 The Loose γ+jets Control Region

The loose γ+jets control region, as well as the photon ID/isolation selection, is described in this section. The γ+jets control region is chosen with the purpose of substituting the loose muon control region used in the 2016 version of this analysis for the calculation of the shape correction scale factors applied to the final estimation of the Z$\rightarrow \nu\bar{\nu}$ background. The γ+jets control region is presumed to be better suited for this estimation due to having a much higher cross-section and therefore, an expected reduction in the statistical and systematic uncertainties associated to the shape correction factors are

expected.

5.3.1 Photon ID and Isolation

Three different working points are provided by the CMS EGM physics object group (POG) for simple cut-based photon identification [**?**]. The three working points, called loose, medium and tight, are chosen according to the requirements of the particular analysis and differ on the amount of background rejection they offer, as well as on their average photon selection efficiency. The higher the efficiency of a given ID, the lower the amount of background that is rejected, and vice-versa. **??** shows the cut values that are applied to photons that are found within both the ECAL barrel and endcap range. The associated values to the efficiency and the background rejection rate are shown for each of the three different photon ID selections.

In order to obtain the high efficiency and background rejection rates shown, a robust set of identification and isolation criteria are selected. A total of five parameters are used for this simple cut based method. For photon identification, the H/E and the $\sigma I\eta I\eta$ variables are found to provide the best results. The H/E parameter is defined as the ratio of the HCAL tower energy over the ECAL seed cluster energy. A threshold value is selected on H/E to remove background from electrons that are detected in both the ECAL and HCAL but have no reconstructed track [**?**]. The $\sigma I\eta I\eta$ variable is known as the photon shower shape variable and is defined in the ECAL as the energy weighted standard deviation of a single crystal within the 5×5 crystal η range, centered around the crystal with maximum energy [**?**]. This variable is a key component in the identification of both electrons and photons since it provides a measure of the shower width where most of the energy has been deposited in a given ECAL crystal.

Table 5.1: Identification and isolation cut values for photons provided by the CMS EGM POG. Values are provided for the three working points described (loose, medium and tight) for both the ECAL barrel and endcaps. The photon selection efficiency of the three working points, as well as their associated background rejection rate, are provided.

Barrel	**Loose (90.06%)**	**Medium (80.19%)**	**Tight (70.01%)**
Background Rejection	**Loose (85.73%)**	**Medium (88.87%)**	**Tight (90.66%)**
H/E	0.105	0.035	0.020
$\sigma I\eta I\eta$	0.0103	0.0103	0.0103
ρ-corrected PF charged hadron isolation	2.839	1.416	1.158
ρ-corrected PF neutral hadron isolation	$9.188 + 0.0126 \cdot p_{\mathrm{T}}^{\gamma} + 0.000026 \cdot p_{\mathrm{T}}^{\gamma 2}$	$2.491 + 0.0126 \cdot p_{\mathrm{T}}^{\gamma} + 0.000026 \cdot p_{\mathrm{T}}^{\gamma 2}$	$1.267 + 0.0126 \cdot p_{\mathrm{T}}^{\gamma} + 0.000026 \cdot p_{\mathrm{T}}^{\gamma 2}$
ρ-corrected PF photon isolation	$2.956 + 0.0035 \cdot p_{\mathrm{T}}^{\gamma}$	$2.952 + 0.0040 \cdot p_{\mathrm{T}}^{\gamma}$	$2.065 + 0.0035 \cdot p_{\mathrm{T}}^{\gamma}$

End Cap	**Loose (90.81%)**	**Medium (80.06%)**	**Tight (70.11%)**
Background Rejection	**Loose (76.90%)**	**Medium (81.50%)**	**Tight (84.34%)**
H/E	0.029	0.027	0.025
$\sigma I\eta I\eta$	0.0276	0.0271	0.0271
ρ-corrected PF charged hadron isolation	2.150	1.012	0.575
ρ-corrected PF neutral hadron isolation	$10.471 + 0.0119 \cdot p_{\mathrm{T}}^{\gamma} + 0.000025 \cdot p_{\mathrm{T}}^{\gamma 2}$	$9.131 + 0.0119 \cdot p_{\mathrm{T}}^{\gamma} + 0.000025 \cdot p_{\mathrm{T}}^{\gamma 2}$	$8.916 + 0.0119 \cdot p_{\mathrm{T}}^{\gamma} + 0.000025 \cdot p_{\mathrm{T}}^{\gamma 2}$
ρ-corrected PF photon isolation	$4.895 + 0.0040 \cdot p_{\mathrm{T}}^{\gamma}$	$4.095 + 0.0040 \cdot p_{\mathrm{T}}^{\gamma}$	$3.272 + 0.0040 \cdot p_{\mathrm{T}}^{\gamma}$

The other three parameters considered, comprise the isolation portion of the photon selection cuts. These are the ρ-corrected particle flow (PF) charged hadron, neutral hadron and photon isolation parameters. As can be seen from **??**, two of these parameters (the neutral hadron and photon isolation) have a dependence on p_{T}^{γ}. These cuts are used to ensure that the identified photon is well isolated within its own cone and by rejecting photons that are identified within close proximity to either a charged or a neutral hadron [**?**]. The value ρ included in the name of each of these parameters refers to the total

pileup density [**?**]. Therefore, the term "ρ-corrected" implies that these values, which are sensitive to the residual contamination that arises from pile-up, have been corrected to include these contributions.

5.3.2 Photon Selection

The event selection process for the γ+jets control region starts with photon candidates that have a $p_{\mathrm{T}} > 200$ GeV and are within the acceptance range of the CMS ECAL (given by $|\eta| < 1.4442$ for the barrel and $1.566 < |\eta| < 2.5$ for the endcaps). The photons are subjected to pass the loose ID/isolation cuts described in **??** in order to remove $\sim 85\%$ of the background processes and obtain a prompt photon sample that is $\sim 90\%$ pure, on average. Additional restrictions include some of the same requirements imposed on the signal baseline selection discussed in **??**. These include $N_j \geq 4$, an $H_{\mathrm{T}} > 300$ GeV, the $\Delta\phi$ requirements for leading jets and the lepton vetoes described in **??**. The lepton veto, in particular, greatly improves the prompt photon selection by removing many of the events in the simulated samples where a lepton gets misidentified as a photon.

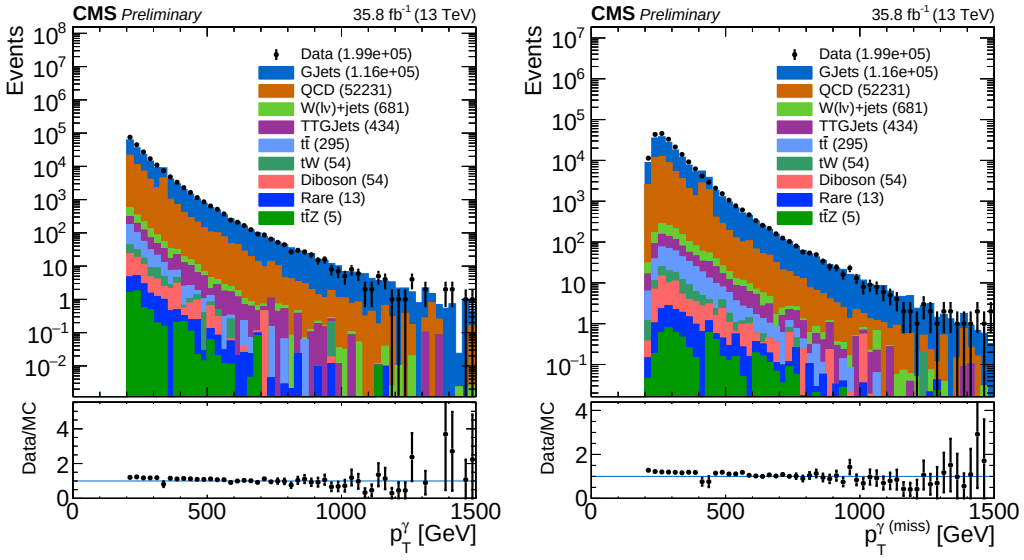

Figure 5.2: Shown are both the p_{T}^{γ} (left) and $p_{\mathrm{T}}^{\gamma(miss)}$ (right) distributions before applying any corrections. $p_{\mathrm{T}}^{\gamma(miss)}$ is obtained by adding the p_{T}^{γ} to the total p_{T}^{miss} in every event.

To further emulate the Z$\rightarrow \nu\bar{\nu}$+jets background, a variable in which the photons are treated as p_{T}^{miss} is defined. We call this variable $p_{\mathrm{T}}^{\gamma(miss)}$ and we obtain it by adding the p_{T}^{γ}

for every event to the total p_{T}^{miss} in the event. Both the p_{T}^{γ} and the resulting $p_{\mathrm{T}}^{\gamma(miss)}$ distributions are shown in **??** as data/MC comparison plots, where the simulated backgrounds are stacked in order of ascending contribution.

The main contributions from simulation arise from the γ+jets, QCD and to a lesser extent, $\mathrm{t\bar{t}}\gamma$. Other non-dominant backgrounds in the control region include contributions from W($l\nu$)+jets, $\mathrm{t\bar{t}}$, Diboson, tW, $\mathrm{t\bar{t}Z}$ and rare processes. Most of these lesser backgrounds are nearly negligible (several orders of magnitude lower than the dominant backgrounds) and are considered to be mostly composed of fake photons. In addition to the cuts described, all of the simulation samples are subjected to weights that apply corrections to pileup as well as the b-tagging efficiency. Data, on the other hand, is obtained from a sample that contains events with at least one identified photon. Photons in this sample are also subjected to the high-level trigger HLT_Photon175, which restricts the selection to photons that have a $p_{\mathrm{T}} > 175$ GeV. Both simulation and data are subjected to the same selection criteria established in this section.

5.3.3 Photon Purity and Fake Rate

Three different types of photons make up the γ+jets CS: prompt photons, produced either directly or through fragmentation, and fake photons. Prompt photons are defined as photons which are formed shortly after the proton-proton collision (i.e. before the produced quarks and gluons have had enough time to form hadrons). Two types of photons fit in this category. The first type, which we designate as direct photons, are photons that are produced directly from the proton-proton interaction [**?**]. A secondary type of prompt photon, that is virtually indistinguishable from the direct photons at the detector level, originates from the decay of π^0 mesons and are called fragmentation photons. The final type of photon found in the CS corresponds to fake (or non-prompt) photons. The fake photon contribution typically arises from leptons (mostly electrons) whose tracks are not properly reconstructed, yet leave energy measurements in the ECAL.

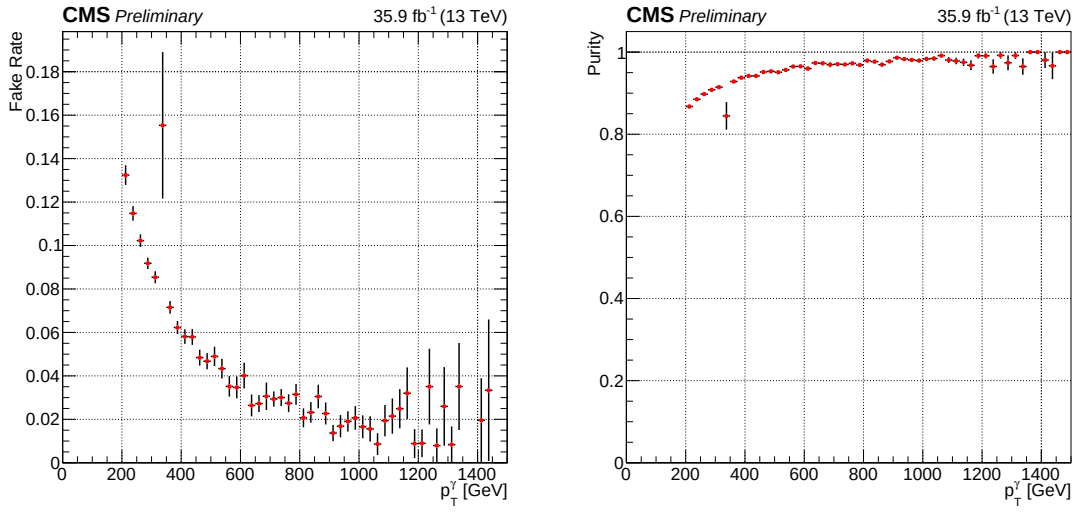

Figure 5.3: Plots for Fake Rate (left) and Purity (right) as a function of the photon p_{T} are shown. The events are selected are required to have a $p_{\mathrm{T}} > 200$ GeV, be within the ECAL acceptance range, and pass the loose ID selection cuts. This selection was produced in order to verify the values given by the E/γ POG. As can be seen, the efficiency (purity) is seen to agree with the values of the loose photon ID/isolation selection.

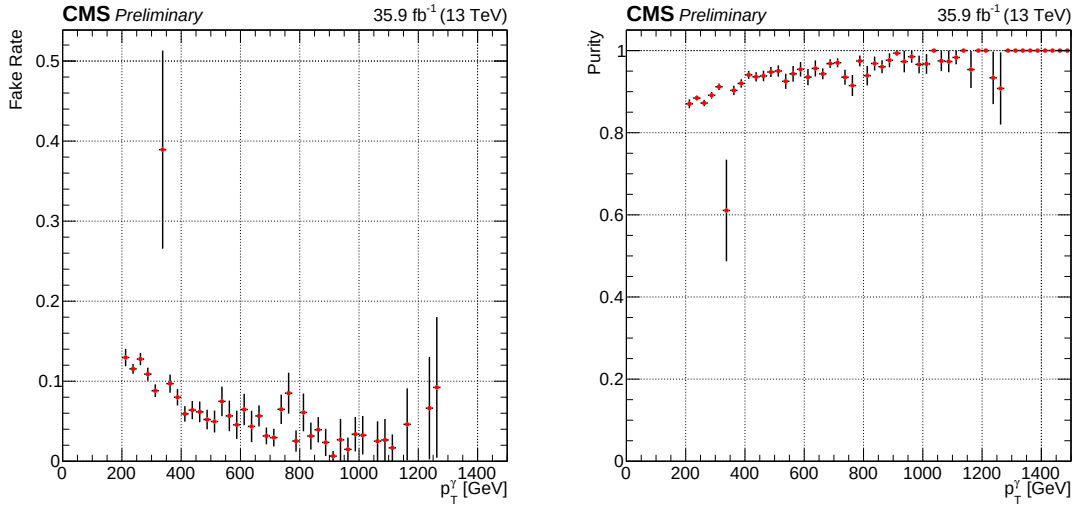

Figure 5.4: Plots for Fake Rate (left) and Purity (right) as a function of the photon p_{T} are shown. These plots include photons with the full control region selection. Aside from exhibiting lower statistics, the plots seem to agree with the fake rate and purity before all the control region cuts are applied.

In order to identify prompt photons, reconstructed photons from the γ+jets and QCD samples are matched to generator-level photons in space and momentum by requiring $\Delta R(\gamma_{\mathrm{gen}}, \gamma_{\mathrm{reco}}) < 0.4$ and $0.5 < p_{\mathrm{T}}^{\mathrm{gen}}/p_{\mathrm{T}}^{\mathrm{reco}} < 2.0$, respectively. Any reconstructed photon which fails to get matched to a generator level photon is labeled as a fake/non-prompt photon. Direct photons are identified by further requiring that the reconstructed photons be matched to a parton (a gluon or quark) in space as $\Delta R(\gamma, \mathrm{parton}) > 0.4$. This require-

ment is intended to distinguish the reconstructed photons from highly boosted π^0's, which compose a large portion of the experimentally indistinguishable fragmentation photons. Finally, fragmentation photons are obtained exclusively from QCD simulation and are required to have $\Delta R(\gamma, \text{parton}) < 0.4$ in order to avoid double counting photons from the γ+jets sample.

With all three types of photons defined, a study can be carried out from simulation to estimate their respective contributions to the defined control region. The study takes into account that any reconstructed photon in the γ+jets or QCD samples can only be categorized as prompt (through direct production or fragmentation) or non-prompt (fake). The purity and fake rate can then be defined in terms of the relative proportions of prompt or non-prompt photons with respect to the sum of the contributions from all three types of photons. Identified direct photons are taken from the γ+jets sample exclusively. Meanwhile, the fragmentation and fake photon contributions are taken from the QCD sample. The three quantities are then added together and their respective contributions are determined in terms of the photon p_{T} (**??**).

The photon purity (**??** and **??**, right) is defined in terms of the prompt and non-prompt photons as:

$$p_\gamma = \frac{prompt}{prompt+fake} \ ,$$

where the prompt photon portion comes from the sum of the direct photons (extracted from the γ+ jets sample) and the fragmentation photons (extracted from the QCD sample). The remaining non-prompt (or fake) photons all come from photons in the QCD sample that were not matched to truth-level photons in space and momentum with the specified required conditions. Meanwhile, the photon fake rate (**??** and **??**, left) is defined from this same combination of samples as:

$$f = \frac{fake}{prompt+fake} \ ,$$

?? shows the purity and fakerate for photons that pass the loose ID/selection, have a $p_{\mathrm{T}} > 200$ GeV and are within the ECAL acceptance range. A sample is obtained in which 77% of the photons are direct, 12% are fragmentation and 11% are fakes. This implies an average purity of ∼89% for this sample, well within the value that is expected. **??** shows the same ratios for the loose γ+ jets control region described in **??**. Although the amount of statistics has decreased due to the additional cuts, a similar trend can be observed.

5.4 The Z→ $\mu^+\mu^-$ Control Region

The Z→ $\mu^+\mu^-$ control region defined in this section is in every respect identical to the one applied in the 2016 analysis (**??**. The only difference between the 2016 method and the one discussed in this chapter is that the Drell-Yan (DY) sample is only used for the normalization correction of the Z→ $\nu\bar{\nu}$ background. Therefore, the loose $\mu\mu$ control region is not used or applied in the calculation of the scale factors. In the following subsections only the tight $\mu\mu$ control region, and its usage to obtain the normalization scale factor R_{norm}, is discussed.

5.4.1 Muon ID and Isolation

The muons are selected using the "medium muon" selection [**?**], per the recommendation of the muon POG. The muon candidates in this selection satisfy $p_{\mathrm{T}} > 10$ GeV and $|\eta| < 2.4$. Other additional cuts are applied to aid in the muon candidate selection, such as an impact parameter cut. Muons are also subjected to a PF relative-isolation (also referred to as mini-isolation) in which the cone size is inversely proportional to the muon p_{T}. This requirement enforces the p_{T} within the isolation cone to be at most 20% of the muon p_{T} in order to eliminate events with an isolated muon. Details of the medium photon selection

are included in **??** and **??**, while details of the impact parameter cut are summarized in **??**.

Muon Medium ID	
Loose muon ID	Yes
Fraction of valid tracker hits >	0.80
Good Global muon OR Tight segment compatibility >	Yes OR 0.451

Table 5.2: Muon Medium ID 2016 HIP Safe

Good Global muon	
Global muon	Yes
Normalized global-track χ^2 <	3
Tracker-Standalone position match <	12
Kick finder <	20
Segment compatibility >	0.303

Table 5.3: Muon Medium ID HIP Safe Good Global Muon

Muon Impact Parameter	
d0 <	0.2
dz <	0.5

Table 5.4: Additional Impact Parameter cut on Muons

5.4.2 Muon Selection in the Tight Control Region

Events are selected from data samples that contain exactly two oppositely charged muons ($\mu^+\mu^-$), which fall within the invariant mass $81 < m_{ll} < 101$ GeV window for the Z boson. Additional cuts for the tight muon selection include baseline requirements such as an $H_{\mathrm{T}} > 300$ GeV, $N_j \geq 4$, the $\Delta\phi$ baseline cut on leading jets, a $p_{\mathrm{T}}^{miss} > 250$ GeV, an $m_{\mathrm{T2}} > 200$ GeV and at least 1 top-tagged jet $N_t \geq 1$. In addition, the p_{T} of the two muons are required to be $p_{\mathrm{T}} > 50$ GeV for the leading muon and $p_{\mathrm{T}} > 20$ GeV for the sub-leading one. The only difference, when compared to the signal region is the missing lepton veto, in addition to the dimuon events being treated as p_{T}^{miss}. This makes for a region that exhibits very similar kinematics to the Z$\rightarrow \nu\bar{\nu}$ signal region, yet suffers from a lack of statistics.

5.5 Analysis

In this section a detailed explanation of the calculation of the scale factors for both shape and normalization corrections is provided. The following methods make use of the loose γ+jets and the tight $\mu\mu$ control regions defined in the previous sections. The procedure involves extracting the shape corrections S_γ from the γ+jets control region and afterwards obtain a single normalization correction factor R_{norm} from the tight $\mu\mu$ control region. Both factors will then be applied to the final prediction of the Z$\rightarrow \nu\bar{\nu}$ background in each of the required search bins.

5.5.1 Shape Correction Using the γ + jets Control Sample

In this section the validation of the γ+jets simulation is discussed in terms of the shape of the loose photon control region. As it was shown in **??**, this control region has high purity for γ+jets events, particularly in regions of high p_{T} ($\gtrsim 300$). In order to apply this correction factor it is assumed that the shape differences between data and simulation are similar between Z$\rightarrow \nu\bar{\nu}$ and γ+jets events. This assumption is validated in studies which compare the cross-section ratio of Z+jets to γ+jets events [**?**]. **??** shows the results of this study, conducted in 2014, for both data and MadGraph simulation with an integrated luminosity of 19.7fb^{-1} and a center-of-mass energy of 8 TeV. It can be seen that for values of $p_{\mathrm{T}}^{Z/\gamma} \gtrsim 300$ GeV, the ratio of the cross-section of both processes becomes nearly constant. It is then a matter of applying a factor to account for the difference in the amount of events between the Z+jets and γ+jets events in order to obtain the total amount of Z$\rightarrow \nu\bar{\nu}$+jets events. This factor is obtained from the tight $\mu\mu$ control region, as shown in **??**.

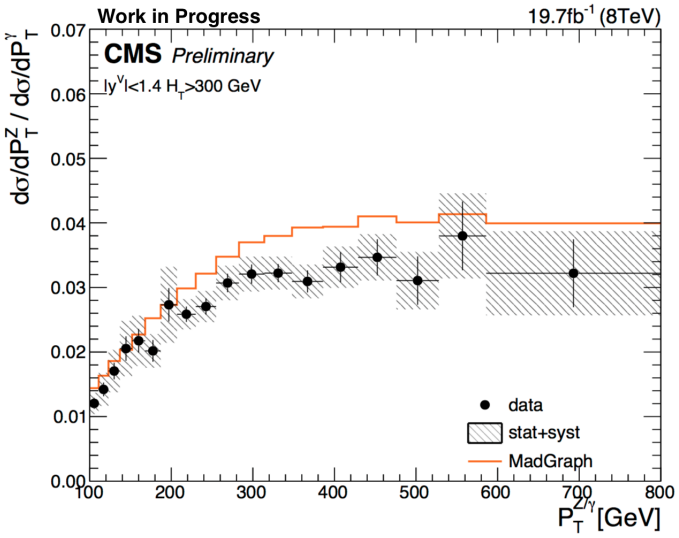

Figure 5.5: Results of study of the Z+jets to γ+jets cross-section ratio for both data and MadGraph simulation. For high values of the vector boson transverse momentum, the ratio between these processes is observed to be nearly constant.

In order to obtain the shape corrections, the ratio between data and simulation of the jet multiplicity distribution is used (**??**). This is due to it exhibiting the highest difference between the observed data and MC. The re-weight for the γ+jets simulation sample is then accomplished by applying the N_{jet} dependent factor $S_\gamma(N_j)$. This scale factor is determined by taking the ratio of the data and simulation, after subtracting all other MC samples from data events:

$$S_\gamma^i = \frac{\text{Data}^i - \text{MC}^i_{\text{other}}}{\text{MC}^i_{\gamma+\text{jets}}},$$

where i denotes any given bin in the N_j distribution. The shape correction factors S_γ^i are displayed graphically in **??** (right) for each N_j bin. These factors correct for differences in the jet multiplicity shape, while the overall normalization is estimated from the tight $\mu\mu$ control region. **??** shows the N_j distribution in the tight $\mu\mu$ control region after the calculated scale factors have been applied. The S_γ correction will be applied to the Z$\rightarrow \nu\bar{\nu}$ simulation final prediction for each of the analysis search bins. The uncertainty associated with the scale factor is estimated from the event yields in the loose photon control region. This uncertainty will form part of the total systematic uncertainty in the final prediction.

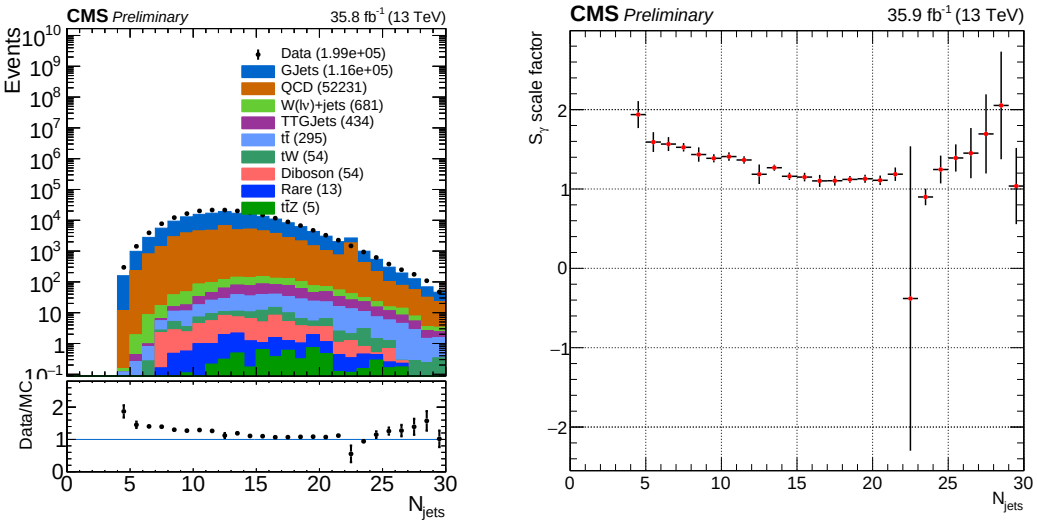

Figure 5.6: Jet multiplicity and the associated S_γ scale factor in the loose photon control region before any corrections are applied.

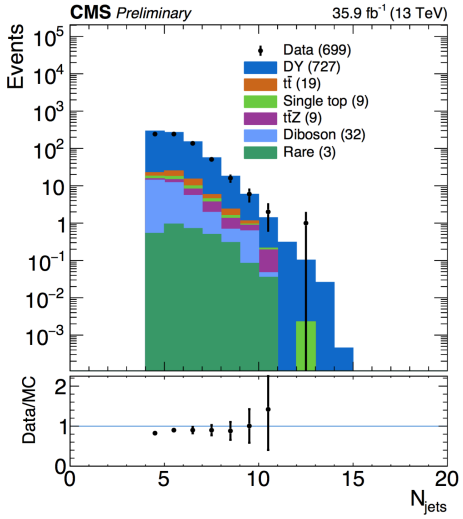

Figure 5.7: N_{jet} distribution in the tight $\mu\mu$ control region after S_γ corrections.

The effect of the $S_\gamma(N_j)$ scale factor is shown for various distributions. These results show that the overall agreement between data and simulation improves after applying the corresponding shape corrections.

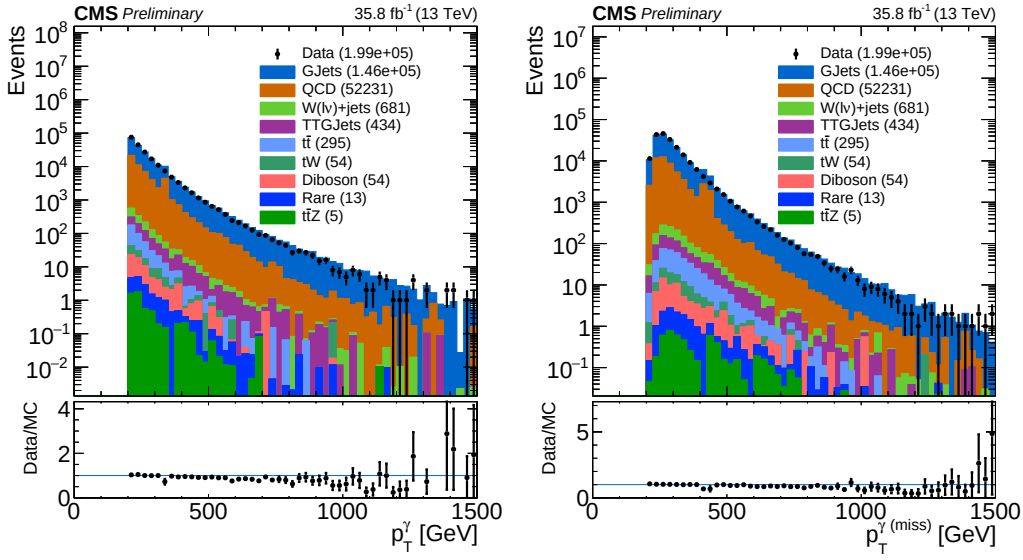

Figure 5.8: p_{T}^{γ} (left) and $p_{\mathrm{T}}^{\gamma(miss)}$ (right) distributions after applying the $S_{\gamma}(N_j)$ scale factor. Comparing to **??**, an improvement in the agreement between data/MC can be observed.

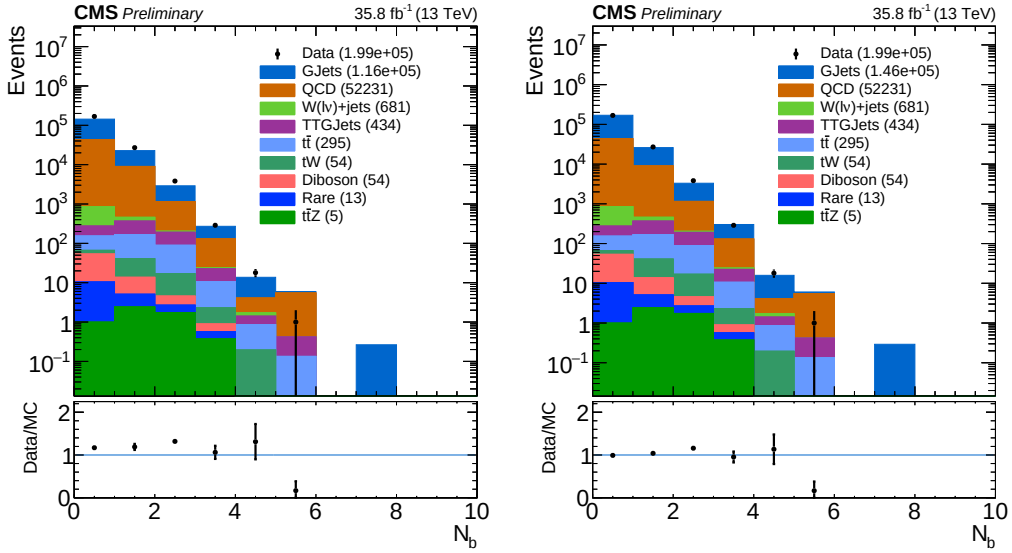

Figure 5.9: N_b distribution before (left) and after (right) applying the $S_{\gamma}(N_j)$ scale factor.

5.5.2 Normalization Correction Using the tight Z$\rightarrow \mu^{+}\mu^{-}$ Control Sample

In order to constrain the normalization of the Z$\rightarrow \nu\bar{\nu}$ simulation sample, a normalization correction factor R_{norm} is calculated from the tight $\mu\mu$ control region defined in **??**. Two categories are considered: the zero b-tagged jet category ($N_b = 0$), and the ≥ 1 b-tagged jet category ($N_b \geq 1$). Both of these categories are statistically consistent with

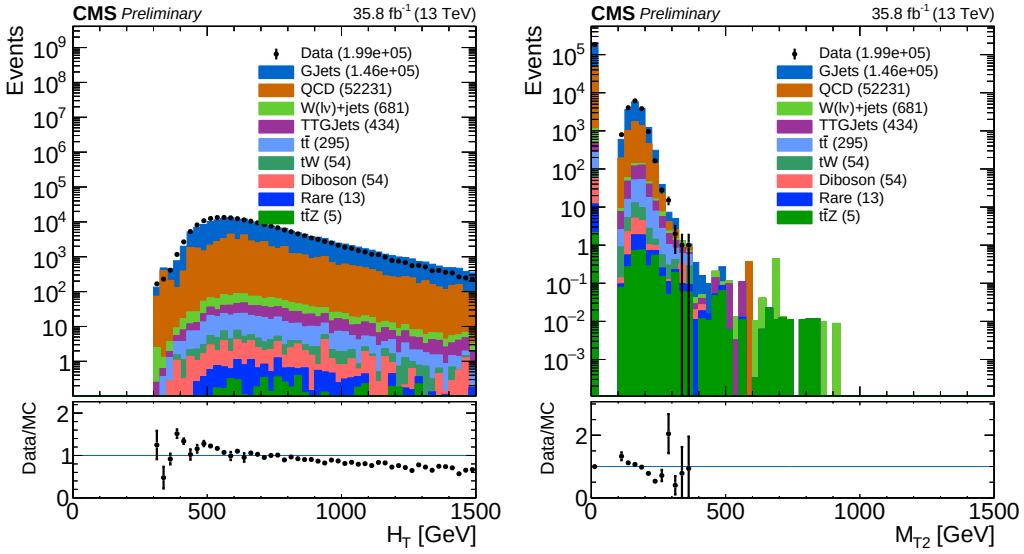

Figure 5.10: H_{T} and m_{T2} distributions applying the $S_{\gamma}(N_j)$ scale factor.

each other but the inclusive region ($N_b \geq 0$) has a lower overall uncertainty. The method used to calculate the normalization scale factor requires that the N_j-dependent shape correction factors already be applied. Then, the R_{norm} factor can be extracted from the ratio of the total event yield in data to that in the simulation. This factor is found to be:

$$R_{norm} = 1.070 \pm 0.085,$$

where the uncertainty includes only the associated statistical uncertainties on data and simulation. This uncertainty is found to be propagated to the final background prediction, see **??**.

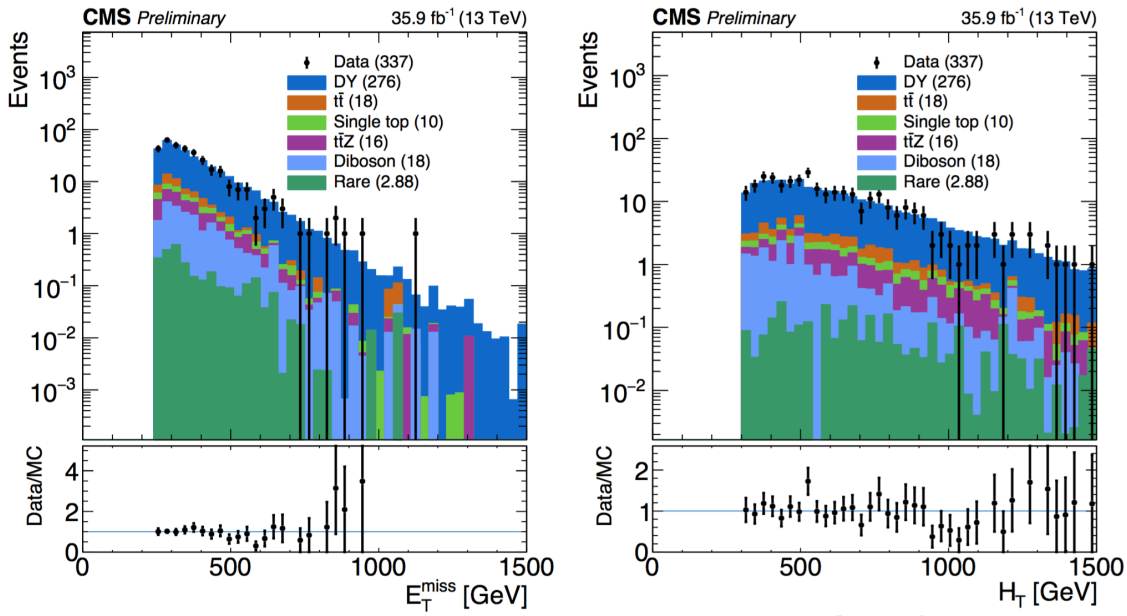

Figure 5.11: Shown are data/MC comparisons for the p_{T}^{miss} (left) and H_{T} (right) distributions after applying both the N_j-dependent shape corrections (S_γ) and the global normalization scale factor (R_{norm}).

Data/MC comparisons are shown in **??** and **??** after applying R_{norm} for several distributions in the study. With this final global scale factor all the required ingredients for the central value of the Z$\rightarrow \nu\bar{\nu}$ background prediction are obtained.

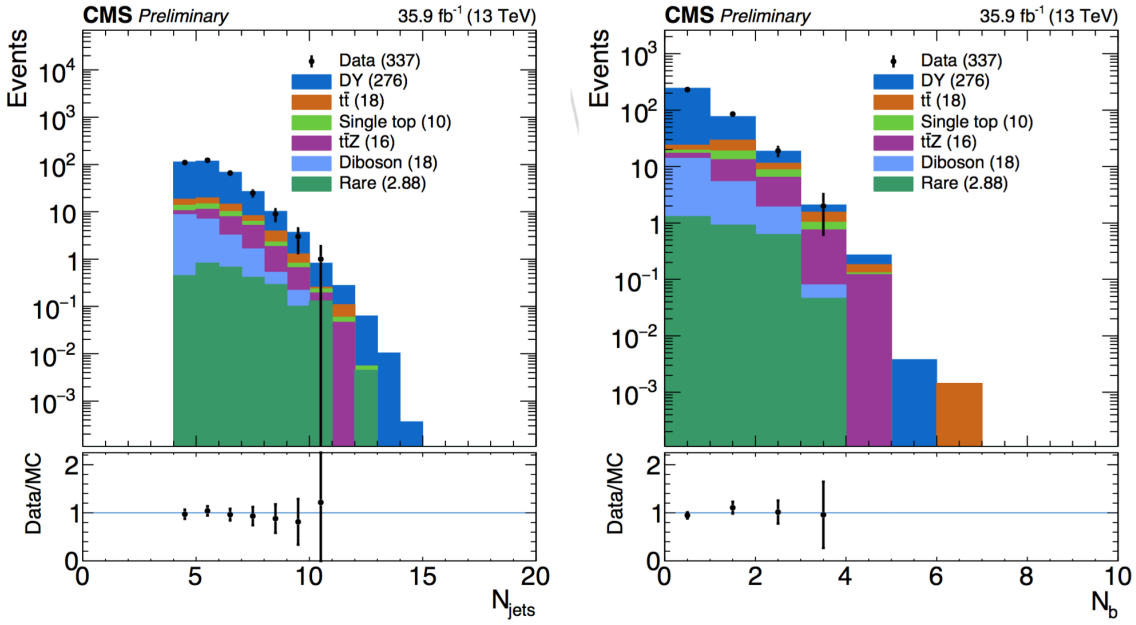

Figure 5.12: Shown are data/MC comparisons for the N_j (left) and N_b (right) distributions after applying both the N_j-dependent shape corrections (S_γ) and the global normalization scale factor (R_{norm}).

5.6 Results

In this section the results for the final estimation of the of the Z$\rightarrow \nu\bar{\nu}$ are presented. The current study includes preliminary results using only data obtained at the CMS detector during 2016. The results for this study are intended to confirm the assumption that the additional γ+jets control region introduced in this analysis reduce the overall uncertainties obtained in the 2016 analyses (described in **??**). Furthermore, this study is intended as a benchmark for future analyses of the SUSY stop group based in Fermilab and will be the method used for the 2017 CMS data.

5.6.1 Systematics

Two categories of uncertainties for the Z$\rightarrow \nu\bar{\nu}$ prediction are considered: uncertainties that are associated to the use of MC simulation and the uncertainties specifically associated to the background prediction method. Several sources are acknowledged in the first category mentioned such as PDF and renormalization/factorization scale choices, jet and p_{T}^{miss} energy scale uncertainties b-tag scale factor uncertainties, and trigger efficiency uncertainties. Given that the simulation sample is normalized to data in the tight control region, uncertainties associated with the luminosity and cross-section are excluded. In addition, the overall Z$\rightarrow \nu\bar{\nu}$ statistical uncertainty from MC simulation is also taken into account.

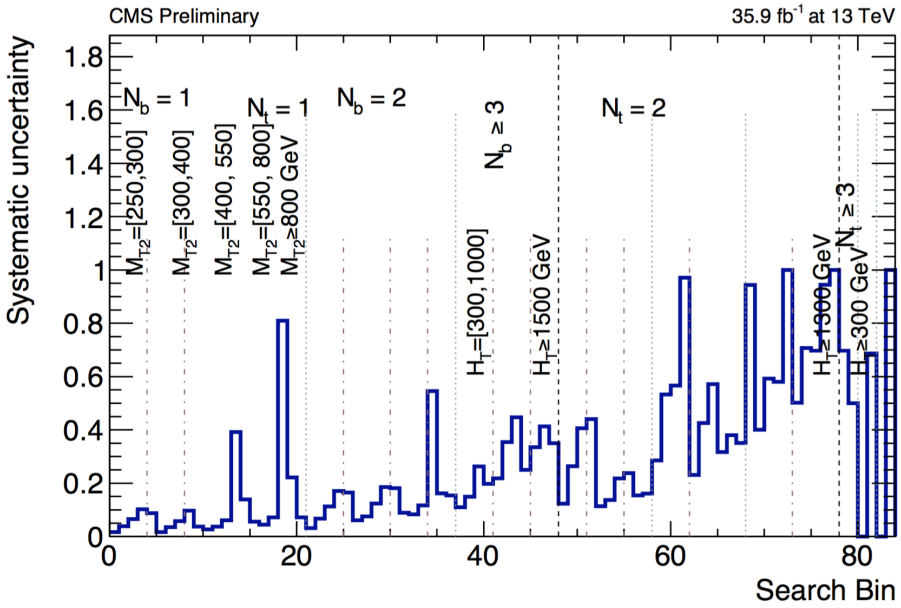

Figure 5.13: Systematic uncertainty in the final prediction, as a function of the search bin, associated to the MC statistics.

The statistical uncertainty associated with each bin in the MC is propagated as a systematic uncertainty. The relative uncertainty per bin can be see in **??**. It shows that the uncertainties for the MC vary from as low as 1% up to 81% and even 100% in some regions. Since the final estimation is scaled using the global normalization factor from the tight $\mu\mu$ control region (R_{norm}), the total uncertainty, due to limited amounts of events in data, is propagated in the final prediction. This is also true for the $S_\gamma(N_j)$ scale factor, in which the residual differences in search variables other than N_j are evaluated in the loose photon control region. Both the uncertainty arising from the N_j re-weighting as well as the residual differences are evaluated together. The uncertainty from R_{norm} is propagated as a flat value of 7.9% uncertainty per each search bin.

5.6.2 Z$\rightarrow \nu\bar{\nu}$ Estimation for the Search Bins

The final estimation for the Z$\rightarrow \nu\bar{\nu}$ background calculated for all 84 search bins is shown in **??**. The statistical uncertainty in bins that have zero events is treated as the average weight (the sum of the weights squared over the weight) times the poisson error on 0 which is 1.8. This average weight is calculated on the basis of a relaxed cut in which $N_b \geq 2$ is required. For comparison, a cut in which $N_t > 2$ where two tops are fake for

584 the Z$\rightarrow \nu\bar{\nu}$ is used.

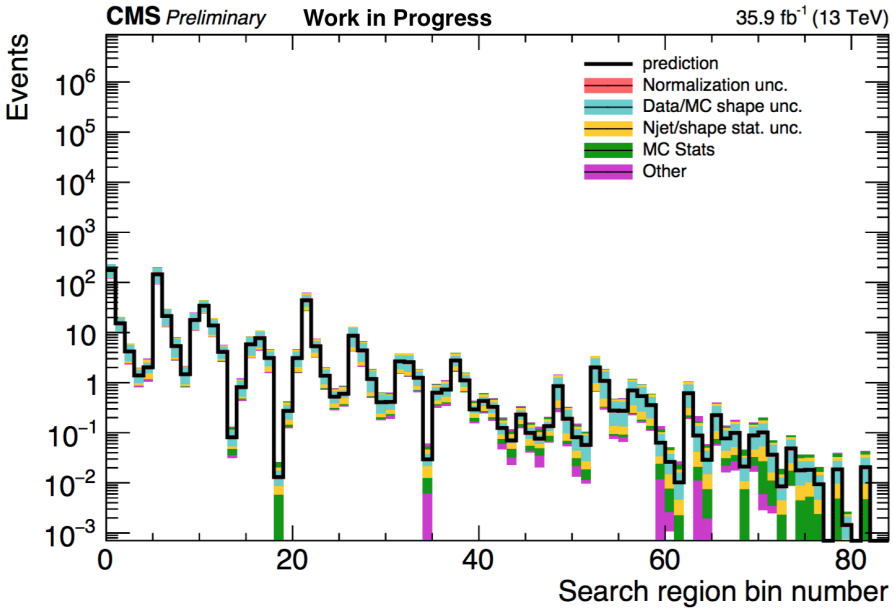

Figure 5.14: Z$\rightarrow \nu\bar{\nu}$ background prediction for all search bins, including the breakdown of the various uncertainties.

Appendix A

Appendix Title

Appendix B

References

[1] CERN, “Processing what to record?,” 2018.

[2] CMS, “The CMS Computing Project,” tech. rep., CERN, 2005.

[3] Coursera, “Machine learning,” 2018.

[4] A. S. Walia, “Types of optimization algorithms used in neural networks and ways to optimize gradient descent,” 2018.